Enhancing thermal properties and moisture resistance of eutectic molten salts via nanoencapsulation for medium-temperature thermal energy storage

Qing Li[1], Songping Mo[1,2,*], Yuxuan Lin[1], Lisi Jia[1,2], Zhi Yang[1,2], Yanping Du[3], Ying Chen[1,2]

1 School of Materials and Energy, Guangdong University of Technology, Guangzhou 510006, China.

2 Guangdong Provincial Key Laboratory on Functional Soft Condensed Matter, Guangdong University of Technology, Guangzhou 510006, China.

3 School of Engineering, Lancaster University, Lancaster LA1 4YW, UK.

Abstract A nanoencapsulation strategy was developed to addresses the limitations of molten salts as phase change materials (PCMs), including leakage and high hygroscopicity, which hinder their practical application in thermal energy storage. An eutectic molten salt $LiNO_3$-$NaNO_3$-KCl (LNK) was first prepared via aqueous solution evaporation, followed by SiO_2 nanoencapsulation using a sol-gel process with methyltriethoxysilane (MTES) and tetraethyl orthosilicate (TEOS) as co-precursors, resulting in nanoencapsulated LNK (NELNK). Characterization results revealed a phase change temperature of 174.7 °C, a supercooling degree of approximately 0 °C, a latent heat of 128.8 kJ/kg, and an encapsulation ratio of 66.2%. NELNK also exhibited excellent thermal cycling stability, retaining 98.3% of its energy storage efficiency after thermal cycles. Moisture absorption tests demonstrated significantly improved moisture resistance compared to the pristine LNK. This work successfully enhances the performance of LNK through modification of the SiO_2 shell, offering a promising solution for medium-temperature thermal energy storage applications.

Keywords: Thermal energy storage; Molten salt; Nanocapsule; Moisture resistance; Phase change material

*Corresponding author. *E-mail address*: mosp@ustc.edu.

Nomenclature

APTES	3-aminopropyltriethoxysilane	TEOS	Tetraethyl orthosilicate
CTAB	Cetyltrimethylammonium bromide	TES	Thermal energy storage
DSC	Differential scanning calorimetry	TGA	Thermogravimetric analysis
EDS	Energy-dispersive X-ray spectroscopy	T_m	Melting temperature
E	Encapsulation efficiency	T_s	Solidification temperature
FT-IR	Fourier transform	W/O	Water-in-oil
H_m	Melting enthalpy, $kJ \cdot kg^{-1}$	XRD	X-ray diffraction
H_s	Solidification enthalpy, $kJ \cdot kg^{-1}$	Greek letters	
LNK	50wt%$LiNO_3$-45wt%$NaNO_3$-5wt%KCl	μ	Viscosity, $kg \cdot m^{-1} \cdot s^{-1}$
MTES	Methyltriethoxysilane	ρ	Density, $kg \cdot m^{-3}$
NELNK	Nanocapsules LNK	ω	Mass fraction
PCMs	Phase change materials	Δ	Change in parameter
R	Encapsulation ratio	Subscripts	
SBO	Soybean oil	l	Latent heat
SEM	Scanning electron microscope	m	Melting
Span 80	Sorbitan oleate	s	Solidification
T	Temperature, K		

1. Introduction

With the continuous growth of global energy demand and the rapid development of renewable energy technologies, thermal energy storage (TES) has received widespread attention due to its unique advantage in effectively addressing the mismatch between energy supply and demand [1, 2]. Among various TES methods, latent heat storage stands out for its high energy storage density and relatively stable phase change temperature during the phase change process. As the medium enabling this technology, phase change materials (PCMs) have demonstrated broad application prospects across diverse fields such as solar energy utilization, industrial waste heat recovery, and building energy efficiency improvement [3-6].

Inorganic PCMs, particularly molten salts, have drawn increasing interest owing to their high latent heat, non-flammability, low vapor pressure, and cost-effectiveness [7]. The advantages make them especially suitable for concentrating solar power systems [8, 9]. However, single-component molten salts often suffer from drawbacks including high melting points, poor thermal stability, and high corrosivity, which limit their practical applicability. To address these issues, eutectic molten salts composed of controlled multi-component ratios have emerged as an effective strategy for optimizing thermophysical properties.

Extensive studies have been conducted on nitrate-based eutectic molten salts. Kenisarin [10] summarized the thermophysical parameters of hundreds of mixed salt systems, highlighting the suitability of nitrate-based PCMs for medium-temperature thermal storage applications. Literature also suggests that the addition of KCl can effectively lower the melting point and expand the operational temperature range of molten salts [11]. For instance, Sang et al [12] developed $NaNO_3$-KNO_3-KCl ternary molten salts with a melting point of 206.12 °C and a latent heat of 110.48 kJk/g. Li et al [13] prepared a novel LNK ternary eutectic salt (50 wt% $LiNO_3$-45 wt% $NaNO_3$-5 wt% KCl) via static fusion, achieving melting and freezing temperatures of 172.4 °C and 141.6 °C, respectively, with a significant supercooling degree of 30.8 °C.

Despite their favorable thermal performance, molten salts face two major practical

challenges: leakage during solid-liquid phase changes and hygroscopicity-induced degradation and corrosion. To mitigate these issues, encapsulation strategies, particularly microencapsulation, have been proposed. Microencapsulation isolates the PCM core from the external environment using a protective shell [14], thereby preventing leakage, enhancing thermal stability, and improving heat transfer efficiency through increased surface area [15].

Considerable research has focused on the thermal properties of phase change microcapsules. Park et al. [16] developed a surfactant-free encapsulation method to synthesize KNO_3@TiO_2 microcapsules, which achieved an encapsulation ratio of approximately 69.4% while maintaining structural stability. Lee et al. [17] employed a sol–gel technique to encapsulate $NaNO_3$ within a SiO_2 shell, attaining an encapsulation efficiency of 85.8%. Zhang et al. [15] applied a limited-water sol-gel process to fabricate KNO_3@SiO_2 microcapsules, achieving a high encapsulation ratio of 95.2% along with good cyclic thermal stability. Ji et al. [18] synthesized Solar Salt (60 wt% $NaNO_3$-40 wt% KNO_3)@SiO_2 microcapsules via sol-gel reaction, resulting in an encapsulation ratio of 60.32%. Pehurajan et al. [19] produced Solar Salt@SiO_2 microcapsules with an encapsulation efficiency of 80.94%, which retained 97.18% of their thermal conductivity after 100 cycles. Wang et al. [20] modified Solar Salt@SiO_2 with CNT-Fe_3O_4 functional materials to develop a novel magnetic microcapsule composite, which exhibited excellent high-temperature stability and cycling performance. Guo et al. [21] demonstrated that Solar Salt@SiO_2 microcapsules are highly compatible with drilling fluids and can be recycled at temperatures up to 220 °C. In summary, although considerable progress has been made in understanding the thermal properties of molten salt microcapsules, their moisture resistance, a critical factor for real-world applications, remains largely unexplored. Addressing this gap is therefore a primary objective of this study.

Moisture absorption poses a significant challenge in the storage and operation of molten salt phase change materials. Exposure to high humidity environments can severely compromise both thermal performance and structural integrity, undermining long-term reliability. Lu et al. [22] reported that a Na_2CO_3/K_2CO_3 composite lost nearly

40% of its thermal capacity after being stored at 80% relative humidity (RH) for 72 h. Similarly, Cabeza et al. [23] reported that NaOH reached a moisture absorption of 20.37% after 8 h of exposure to 70% RH at 19 °C. In another study, Deng et al. [24] observed a notable decline in thermal conductivity under 50 - 80% RH conditions. These findings underscore the urgent need to enhance the moisture resistance of molten salt PCMs. While some efforts have been made, such as Mo et al.'s preparation of $LiNO_3$/NaCl@SiO_2 nanocapsules [25], the hygroscopicity remains problematic. Encapsulation offers a promising solution, but more effective strategies are required.

Silica (SiO_2), a widely used shell material, is commonly synthesized via the hydrolysis and condensation of precursors such as tetraethyl orthosilicate (TEOS) [20, 26]. However, TEOS-derived SiO_2 often exhibits brittleness [27], which are unsuitable for highly hygroscopic molten salts [28]. In contrast, methyltriethoxysilane (MTES), a silane coupling agent, has demonstrated significant potential for enhancing the hydrophobicity of silica-based materials. Several studies have employed MTES as a co-precursor to tailor the surface properties of silica gels and coatings. For instance, Liu et al. [29] fabricated hydrophobic silica aerogels via a sol–gel process using TEOS and MTES as co-precursors, emphasizing that a sufficient amount of MTES is essential to achieve effective hydrophobicity. Dudas et al. [30] synthesized silica aerogels with varying MTES/TEOS molar ratios and demonstrated that increasing the MTES content reduces the number of surface silanol groups, and the reduction in –OH groups decreased surface hydrophilicity. Similarly, Darmawan et al. [28] developed a hydrophobic silica coating from MTES to improve the water resistance of ceramic tiles. In a follow-up study, they established that the hydrophobicity of silica layers is proportional to the number of Si–CH_3 groups and inversely proportional to the number of Si–OH groups [31]. These findings collectively demonstrate that incorporating MTES as a co-precursor enables tunable control over material hydrophobicity, a key attribute that positions MTES as a highly promising candidate for enhancing the moisture resistance of molten salt microcapsules.

Beyond hydrophobicity, MTES has also been explored as a silica precursor to improve shell integrity, particularly in mitigating leakage and enhancing mechanical

robustness. For instance, Fei et al. [32] employed MTES as a modifier in Pn@SiO_2 microcapsules, achieving a 20.53% reduction in leakage rate, which was attributed to the elasticity imparted by methyl groups integrated into the silica network. Similarly, Lin et al. [33] fabricated stearic acid microcapsules via co-hydrolysis of MTES and TEOS, and found that leakage was effectively prevented when the MTES content exceeded that of PCM, while maintaining a high enthalpy of 179.29 kJ/kg. Despite its considerable promise as a precursor, the potential of MTES for encapsulating highly hygroscopic molten salts remains unexplored. To address this gap, the present study introduces MTES as a co-precursor alongside TEOS to encapsulate hygroscopic molten salts, offering a novel strategy to significantly enhance moisture resistance.

This work presents a pioneering approach to overcoming the inherent limitations of hygroscopic molten salts by developing nanoencapsulated molten salts with simultaneously improved thermal and environmental resilience. The eutectic salt LNK was first synthesized via an aqueous solution method followed by controlled evaporation, yielding a homogeneous eutectic with markedly suppressed supercooling and thermophysical properties surpassing those of conventional Solar Salt. MTES and TEOS were then co-utilized as silica precursors to fabricate the nanoencapsulated LNK (termed NELNK). The resulting nanocapsules were comprehensively characterized with respect to microstructure, crystal structure, chemical composition, mechanical properties, phase change behavior, thermal and cycling stability, surface hydrophobicity and moisture resistance performance. Collectively, this study establishes a pathway to enhance the durability and real-world applicability of hygroscopic molten salts, particularly in high-humidity environments.

2 Materials and methods

2.1 Materials

All chemicals used in the synthesis of nanocapsules were of high purity and analytical grade, as listed in Table 1. These reagents were employed without further purification. They are commonly utilized in chemical synthesis and analytical testing.

Table 1 Experimental chemicals.

Chemical	Purity	Manufacturer
$LiNO_3$	99%	Shanghai Aladdin Biochemical Technology Co., Ltd.
$NaNO_3$	99%	Shanghai Aladdin Biochemical Technology Co., Ltd.
KCl	99%	Shanghai Aladdin Biochemical Technology Co., Ltd.
$NH_3 \cdot H_2O$	25%	Guangzhou Chemical Reagent Company
Soybean oil (SBO)	Analytic reagent	Shanghai Aladdin Biochemical Technology Co., Ltd.
Sorbitan oleate (Span80)	Chemically Pure	Sigma-Aldrich Reagent Co., Ltd.
Cetyltrimethylammonium bromide (CTAB)	99%	Shanghai Macklin Biochemical Co., Ltd.
TEOS	Analytic reagent	Tianjin Damao Reagent Co., Ltd.
MTES	98%	Shanghai Aladdin Biochemical Technology Co., Ltd.
N-hexane	Analytic reagent	Tianjin Zhiyuan Chemical Reagent Co., Ltd.

2.2 Preparation of LNK eutectic salt

To minimize moisture, $LiNO_3$, $NaNO_3$, and KCl were pre-dried at 120 °C for 2 h before use. A total of 10 g of LNK eutectic salt was prepared by dissolving the respective salts in 50 mL of deionized water under magnetic stirring at 600 rpm for 1 h. The solution was then transferred to an oil bath at 120 °C to evaporate the water completely. Subsequently, the residue was heated on a hot plate at 300 °C for 4 h to ensure full melting and homogenization. The melt was rapidly cooled, solidified, and ground into fine powder. Finally, the sample was dried at 120 °C for 3 h and stored in a sealed container for subsequent use. The recrystallization process effectively reduced the particle size of the molten salt, which is critical for obtaining nanocapsules with small and uniform particle size.

2.3 Synthesis of LNK nanocapsules

NELNK were synthesized using a water-in-oil (W/O) inverse emulsion sol–gel method. First, the oil phase was prepared by dissolving 0.6 g of Span 80 in SBO, followed by continuous stirring at 60 °C for 30 min. For the aqueous phase, 10 g of the LNK eutectic salt was dissolved in a minimal amount of deionized water and stirred at room temperature for 15 min until fully dissolved. Then, 0.15 g of CTAB surfactant was added to ensure uniform mixing. Ammonia was introduced to create an alkaline environment favorable for the sol–gel reaction.

Next, the aqueous phase was slowly added dropwise into the oil phase under vigorous stirring to form a stable W/O inverse emulsion. MTES and TEOS were used as silica precursors. The precursor mixture was injected into the emulsion at a rate of 350 μL/min using a syringe pump, and the reaction was carried out at 60 °C for 8 h. After the reaction, the resulting solid-liquid mixture was washed multiple times with hexane, and the white precipitate was collected via centrifugation. Finally, the product was freeze-dried for 24 h to obtain the NELNK. The detailed compositions of the precursors are summarized in Table 2.

Table 2 Formulations used to prepare NELNK

Sample	Precursors TEOS(ml)	Precursors MTES(ml)
NELNK-1	9	5
NELNK-2	9	4
NELNK-3	9	3
NELNK-4	9	2
NELNK-5	8	2
NELNK-6	10	2
NELNK-7	11	2

2.4 Characterization of NELNK

The morphology and microstructure of the samples were examined using scanning electron microscopy (SEM). To enhance conductivity and prevent charge accumulation, each sample was coated with a thin layer of gold prior to imaging.

Particle size distribution was measured using a particle size analyzer (DelsaNano C, Beckman Coulter, USA).

The structure and shell thickness of the nanocapsules were determined using transmission electron microscopy (TEM; FEI, Tecnai G2 F30 S-Twin).

X-ray diffraction (XRD, D/max-Ultima, Rigaku, Japan) was employed to characterize the crystalline structures of LNK and NELNK over a 2θ range of 10°–90°, with a scanning speed of 10 °/min.

Fourier transform infrared spectroscopy (FT-IR, Nicolet 6700, Thermo Fisher Scientific, USA) was conducted to investigate chemical structure and functional group changes in the range of 400–4000 cm^{-1}.

The shell flexibility of the nanocapsules was evaluated using atomic force microscopy (AFM, Bruker, Germany). Prior to measurement, samples were dispersed in deionized water, and a droplet was deposited onto freshly cleaved mica and air-dried under ambient conditions. All measurements were performed using a RTESPA-300 probe, with the spring constant and deflection sensitivity calibrated prior to testing. The nanocapsules were positioned on the AFM stage, aligned with the optical axis, and subjected to nanoindentation at a feed rate of 100 nm/s. Force–displacement (F–S) curves were collected from multiple locations across the capsule surface, with a maximum applied load of 30 nN, enabling quantitative assessment of shell flexibility.

Thermal properties of the nanocapsules were evaluated by differential scanning calorimetry (DSC, DSC3 STAR, Mettler Toledo, Switzerland). Samples were heated from 100 °C to 250 °C at a rate of 10 °C/min under a nitrogen atmosphere (flow rate: 50 mL/min). Prior to measurement, thermal history was removed by heating the samples to 250 °C at 50 °C/min and holding for 5 min. Key thermal parameters were extracted from the DSC thermograms.

Thermogravimetric analysis (TGA) was performed to assess thermal stability over a temperature range of 50–800 °C at a heating rate of 10 °C/min under nitrogen purge (20 mL/min).

Thermal reliability was tested using a muffle furnace. Dried NELNK samples were subjected to repeated heating and cooling cycles between 30 °C and 190 °C at a rate of 10 °C/min, with a 5-min hold at 190 °C. Phase change behavior was analyzed after every ten cycles.

The hydrophobicity of the nanocapsules was determined by a contact angle tester (DSA100, KRUSS, Germany), in which the nanocapsules were first adhered to a slide, and then a drop of water was added to the surface of the sample to determine the contact angle within one minute. To ensure the accuracy of the data, three measurements were taken on the same sample and the average value was taken as the experimental result.

3 Results and discussions

3.1 Reaction process and mechanism of NELNK

The synthesis mechanism of NELNK is illustrated in Fig. 1. The process primarily involves the formation of a W/O emulsion system, followed by the hydrolysis and condensation of silica precursors at the oil–water interface.

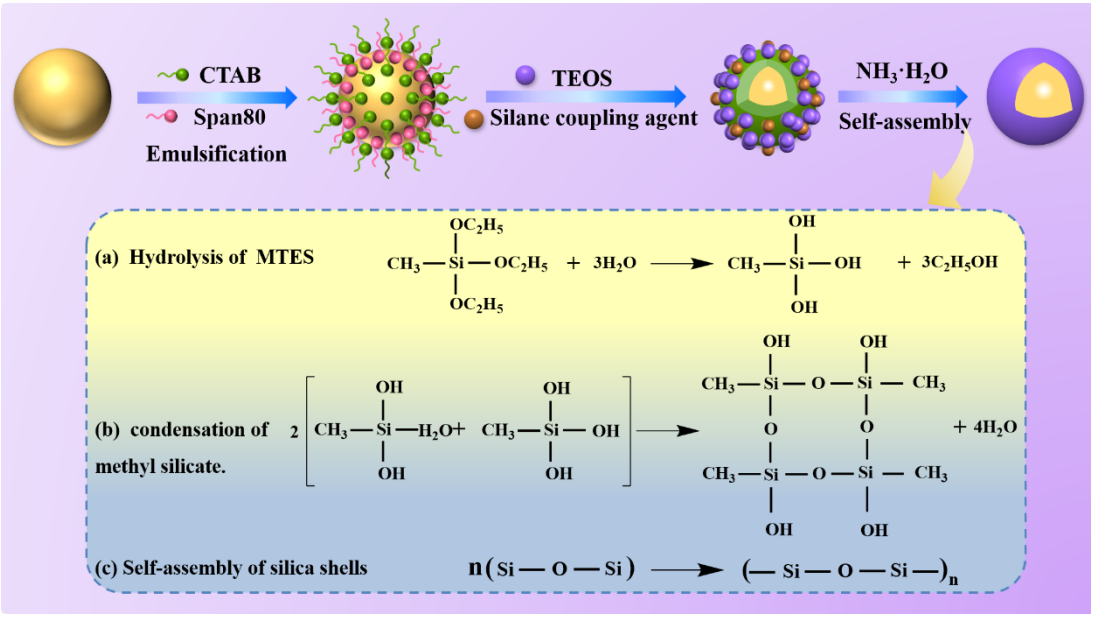

Fig. 1. Synthesis mechanism of NELNK

First, LNK salt and the hydrophilic surfactant CTAB were dissolved in deionized water and magnetically stirred to form a homogeneous aqueous phase. This solution was then dispersed into an oil phase composed of SBO and the lipophilic surfactant Span 80. Under high-speed shear mixing, the surfactant molecules self-assembled at the droplet interface: the hydrophilic head oriented toward the aqueous droplet containing LNK, while the hydrophobic tail extended into the continuous oil phase, effectively stabilizing the LNK droplets and forming a uniform W/O emulsion.

Subsequently, a pre-mixed silica precursor solution consisting of MTES and TEOS was added dropwise into the emulsion under constant stirring at 60 °C. Ammonia was introduced earlier to establish an alkaline environment (pH ~9–10), which significantly influences the reaction kinetics. Initially, TEOS undergoes rapid hydrolysis under acidic conditions to produce silanol (Si–OH) and methylsilanol (Si–OCH_3) monomers [34]. However, as the pH increases due to ammonia addition, the hydrolysis rate decreases while the condensation rate increases, allowing the silanol groups to polymerize and form a three-dimensional Si–O–Si network around the LNK droplets [35].

Silanol monomers are enriched at the oil–water interface via hydrogen bonding with the hydrophilic segments of CTAB. As the condensation progresses, these monomers assemble around the LNK droplets, eventually forming a dense and continuous SiO_2 shell. This in situ encapsulation successfully constructs the core–shell structure of NELNK.

3.2 Microscopic morphology and particle size distribution of NELNK

3.2.1 Microscopic morphology

Fig. 2 presents SEM images of NELNK samples synthesized under varying MTES/TEOS ratios. The effects of precursor composition on nanocapsule morphology and structural integrity were systematically investigated.

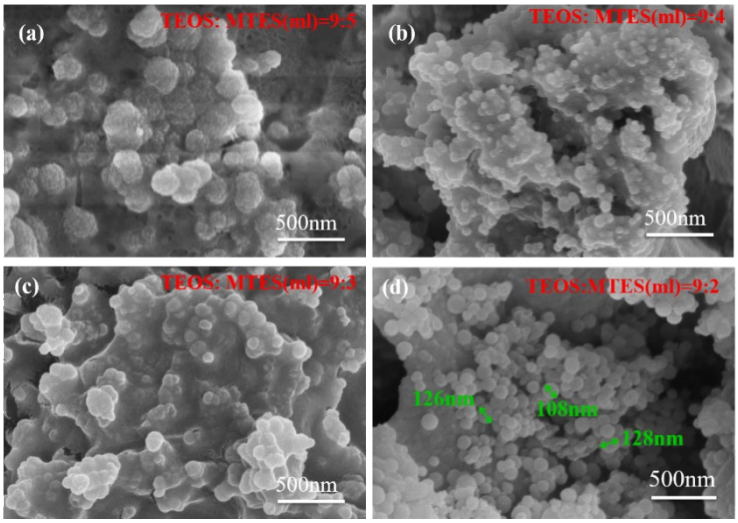

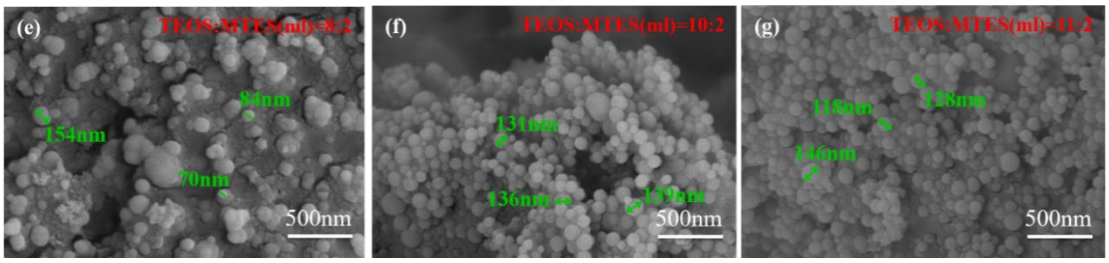

Fig. 2 SEM images of nanocapsules: (a) NELNK-1, (b) NELNK-2, (c) NELNK-3, (d) NELNK-4, (e) NELNK-5, (f) NELNK-6, (g) NELNK-7. The annotated particle sizes represent typical dimensions.

Fig. 2(a–d) shows SEM images of NELNK-1 to NELNK-4, prepared with a constant TEOS amount but decreasing MTES content (from 5 mL to 2 mL). At higher MTES concentrations (e.g., 5 mL), the samples exhibit rough surfaces and irregular morphologies. As previously reported by Zhang [36], Alva [34] and others, excess MTES results in rough silica surfaces, which can be attributed to steric hindrance effects that reduce the condensation efficiency of silica precursors [37]. As the MTES content decreased, the surface morphology became smoother. Notably, at the lowest MTES volume tested (2 mL; Fig. 2d), the nanocapsules display a regular, well-defined morphology, smooth surfaces, and minimal agglomeration. A narrow particle size distribution is observed, with typical diameters ranging from approximately 108 to 128 nm (corresponding to the particles marked in green in the image). This suggests that reducing the MTES content enhances shell densification and improves structural integrity. Therefore, an MTES dosage of 2 mL yields microcapsules with optimal morphological characteristics.

To further optimize the formulation, samples NELNK-5 to NELNK-7 were synthesized using a fixed MTES dosage of 2 mL and varying TEOS volumes of 8 mL, 10 mL, and 11 mL, respectively (Figs. 2(e)–2(g)). Together with NELNK-4, these samples formed a controlled series designed to systematically evaluate the influence of TEOS content on nanocapsule morphology and particle size. All four samples exhibited well-defined spherical structures with smooth surfaces. For quantitative size analysis, particle diameters were measured from SEM images using ImageJ software; results are annotated in Fig. 2. Notably, samples NELNK-1 to NELNK-3 were excluded from size

measurements due to the absence of clearly discernible spherical morphologies.

As shown in Fig. 2, a clear trend toward improved size uniformity emerges as TEOS volume increases from 8 mL to 11 mL: NELNK-5 (8 mL TEOS) displays irregular particle sizes, whereas NELNK-6 (10 mL) and NELNK-7 (11 mL) exhibit highly uniform spherical morphologies. However, increasing TEOS beyond an optimal threshold does not enhance overall performance, in fact, excess TEOS negatively impacts the encapsulation ratio, as discussed in Section 3.5.

Collectively, this analysis reveals that MTES governs nanocapsule formation: excessive MTES (3–5 mL) introduces steric hindrance that disrupts SiO_2 shell assembly, while 2 mL promotes smooth, uniformly sized spheres. In contrast, TEOS primarily modulates particle shape: insufficient TEOS yields irregular morphologies, while surplus TEOS compromises encapsulation ratio.

Based on comprehensive morphological and dimensional assessments, NELNK-4, NELNK-6, and NELNK-7, which all exhibit uniform spherical morphology and narrow size distributions, were selected for subsequent DSC analysis to evaluate their TES performance.

3.2.2 Particle size distribution

Although some aggregation was observed in SEM images, this is likely due to capillary forces during freeze-drying rather than true interparticle adhesion. The particle size of NELNK-6 was further characterized using a particle size analyzer. Prior to measurement, the nanocapsules were diluted with deionized water and subjected to 30 min of ultrasonication to prevent aggregation. As shown in Fig. 3(a), 99.3% of NELNK was distributed below 400 nm, and Fig. 3(b) reveals that the particle size distribution of NELNK-6 was centered at 167 nm. The particle size of the nanocapsules obtained by the particle size distribution test matched the results showed by SEM (Fig. 2), which indicated that they had good monodispersity.

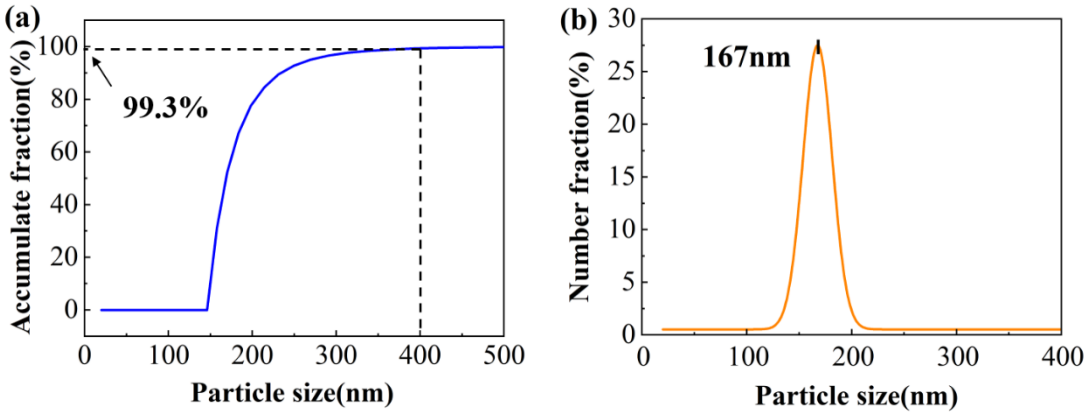

Fig. 3 (a) single particle size distribution and (b) cumulative particle size distribution of NELNK-6

3.2.3 Shell thickness

To elucidate the core–shell structure and quantify shell thickness, the representative sample NELNK-6 was further analyzed by TEM. As shown in Fig. 4(a), NELNK-6 displays a well-defined core–shell morphology with an overall diameter of approximately 150 nm. The dark core corresponds to the LNK phase, while the surrounding lighter contrast ring represents the silica shell. The contrast interface between core and shell confirms successful and complete encapsulation. A higher-magnification image (Fig. 4(b)) reveals a uniform shell thickness of about 20 nm, underscoring the success of the encapsulation process.

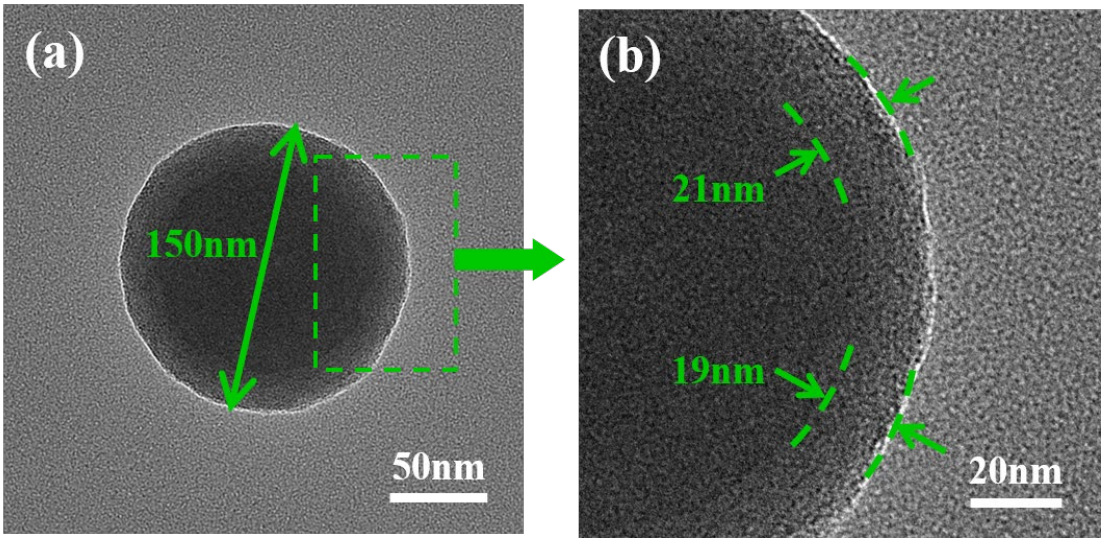

Fig. 4 TEM images of NELNK-6

3.3 Crystal structure analysis of NELNK

Fig. 5 presents the XRD patterns of pure LNK, SiO_2, and three representative NELNK samples. Pure SiO_2 exhibited no distinct diffraction peaks, confirming its amorphous nature. In contrast, LNK showed multiple sharp diffraction peaks corresponding to $NaNO_3$ (JCPDS No. 85-0850), $LiNO_3$ (JCPDS No. 80-0203), and KCl (JCPDS No. 78-0656), with no impurity phases detected. This confirms the high purity and chemical compatibility of the ternary eutectic salt prepared via the evaporation method.

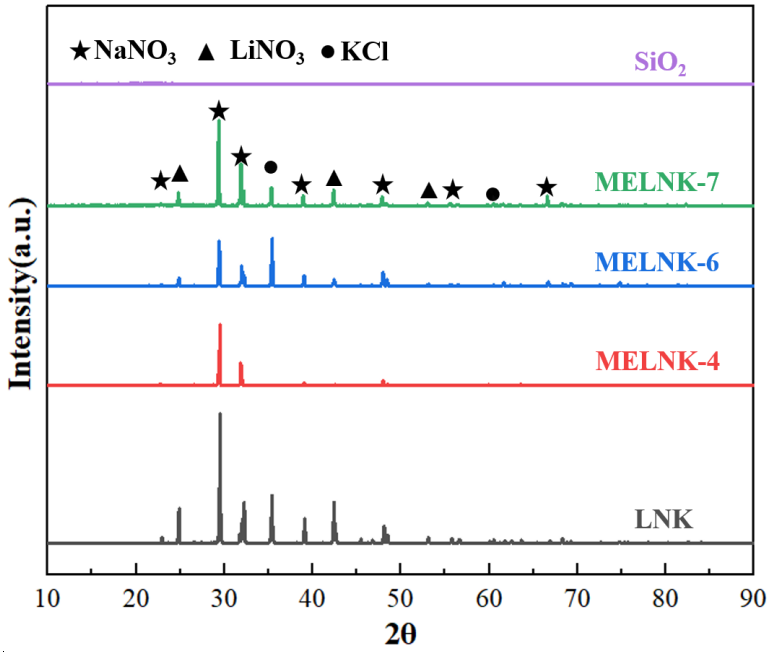

Fig. 5 XRD plots of LNK and NELNKs

Importantly, all characteristic diffraction peaks of LNK were retained in the NELNK samples, with no peak shifts observed, indicating that the crystalline structure of the core material remained intact after encapsulation. The slight reduction in peak intensity can be attributed to the scattering effect of the amorphous SiO_2 shell and possible spatial confinement effects within the nanocapsule structure.

These results demonstrate that the nanoencapsulation process does not induce chemical reactions or structural distortions in the LNK core, preserving its thermophysical properties for subsequent applications.

3.4 Chemical Composition Analysis of NELNK

Fig. 6 presents the FTIR spectra of pure SiO_2, LNK eutectic salt, and three NELNK samples with intact shells. All spectra exhibit a broad absorption band around 3450 cm^{-1}, attributed to the O–H stretching vibration of adsorbed water molecules [38]. This feature arises from two sources: (1) the high hygroscopicity of the LNK salt, which readily absorbs moisture from the ambient environment, and (2) the presence of residual silanol groups (Si–OH) on the surface of the SiO_2 shell, which are also prone to water adsorption under humid conditions [39]. These combined effects contribute to the enhanced intensity of the O–H stretching peak.

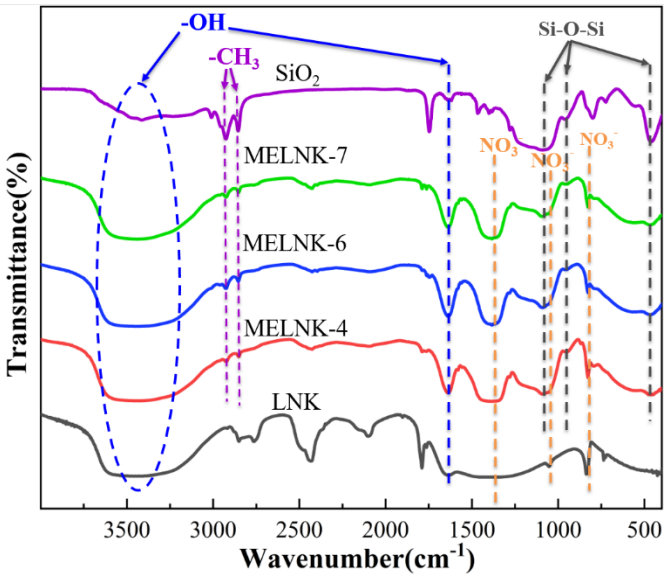

Fig. 6 FTIR plots of SiO_2, LNK molten salt and NELNKs

The FTIR spectra of both LNK and NELNK display characteristic absorption bands at 825 cm^{-1}, 1051 cm^{-1}, 1384 cm^{-1}, which correspond to the out-of-plane deformation, symmetric stretching, and asymmetric stretching modes of nitrate ions, respectively [40, 41]. Two strong absorption peaks at 2973 cm^{-1} and 2890 cm^{-1} represent the symmetric stretching vibration of $–CH_3$ group [30, 38]. These results indicate that the core components of LNK remain chemically unchanged after encapsulation.

For the SiO_2 sample, the sharp peak at 470 cm^{-1} is due to the Si-O-Si bending vibration vibrations. The two distinct peaks at 960 cm^{-1} and 1078 cm^{-1} are associated with the symmetric and antisymmetric stretching vibrations of Si–O–Si bonds, respectively [42]. Additionally, the peak at 1631 cm^{-1} corresponds to the bending

vibration of surface silanol groups (Si–OH) [43].

Importantly, the FTIR spectra of the NELNK retain all the characteristic peaks of both LNK and SiO_2, without any new absorption bands appearing. This confirms that the nanocapsules consist solely of LNK and SiO_2, with no evidence of chemical reactions occurring between the core material and the shell during the encapsulation process. The interaction between the two components is therefore physical in nature. These findings further validate that LNK was successfully encapsulated within the SiO_2 shell without structural or chemical degradation.

3.5 Mechanical properties analysis

The Young's modulus of the shell material is a key parameter governing the mechanical behavior of nanocapsules, as it quantifies material stiffness: a lower Young's modulus corresponds to a more flexible structure. Fig. 7(a) presents a schematic of the nanoindentation tests performed on the nanocapsules. To ensure reliability and minimize random errors, 20 force–displacement (F–δ) curves were collected for each sample. The loading segments of these curves were analyzed using the Hertz contact model [44], which describes the indentation force (F) applied to an elastic material:

$$F = \delta^2 \frac{\pi}{2} \frac{E}{(1 - v^2)} \tan\alpha \tag{1}$$

where δ, v, α, and E represent the indentation depth, Poisson's ratio, opening angle of the AFM probe tip, and the Young's modulus, respectively. The experimental F–δ curves were well fitted by a parabolic function, with high correlation coefficients (r^2>0.99) consistently observed. Only datasets with $r^2 \geqslant 0.98$ were included in the analysis.

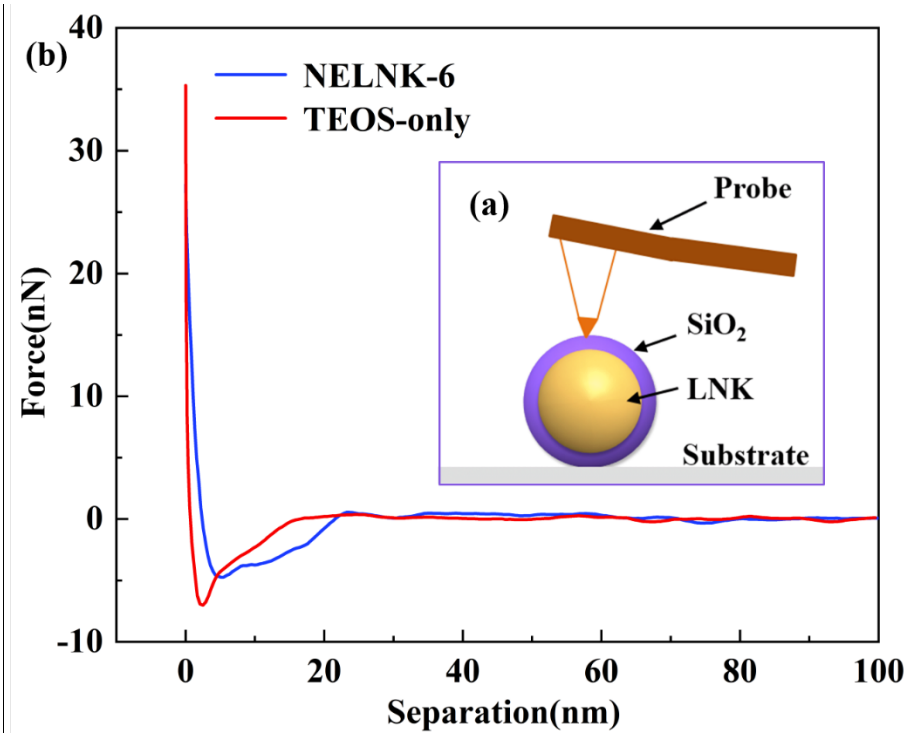

Fig. 7 (a) Representative AFM force–distance curve; (b) Schematic illustration of nanoindentation test

Figure 7(b) displays representative force–displacement curves obtained from probe retraction for both MTES-modified NELNK-6 and TEOS-only nanocapsules. For clarity, "TEOS-only" refers to LNK@SiO_2 nanocapsules synthesized using 10 mL of TEOS as the sole silica precursor, without any MTES; this sample serves as the benchmark for comparison. The significantly reduced slope in the contact region of the NELNK-6 sample indicates a marked decrease in Young's modulus, reflecting enhanced elastic deformability. This observation is further confirmed by quantitative results: the average Young's modulus of the TEOS-only nanocapsules is 18.430 GPa, whereas MTES-modified NELNK-6 exhibits a dramatically lower value of 1.750 GPa. This ~90% reduction underscores the profound softening effect of MTES incorporation, demonstrating that MTES modification effectively enhances flexibility of the silica shell.

This improvement is primarily attributed to the incorporation of non-hydrolyzable methyl (–CH_3) groups from MTES into the silica network. In contrast to TEOS, which fully hydrolyzes to form cross-linked, rigid Si–O–Si frameworks, the presence of methyl groups results in a more flexible organic–inorganic hybrid structure.

This enhanced flexibility implies that NELNK nanocapsules are far less susceptible to cracking under repeated thermal cycling. Consequently, their long-term structural integrity is significantly improved, contributing to extended service life and demonstrating strong potential for deployment in demanding real-world applications, particularly within concentrating solar power and other advanced TES systems.

3.6 Phase change characterization

3.6.1 Phase change behavior of LNK

Fig. 8 presents the DSC curves of the LNK eutectic salt during melting and freezing processes. The DSC profiles exhibit a single dominant peak in both heating and cooling scans, indicating that all components fully participate in the eutectic crystallization, with no phase separation.

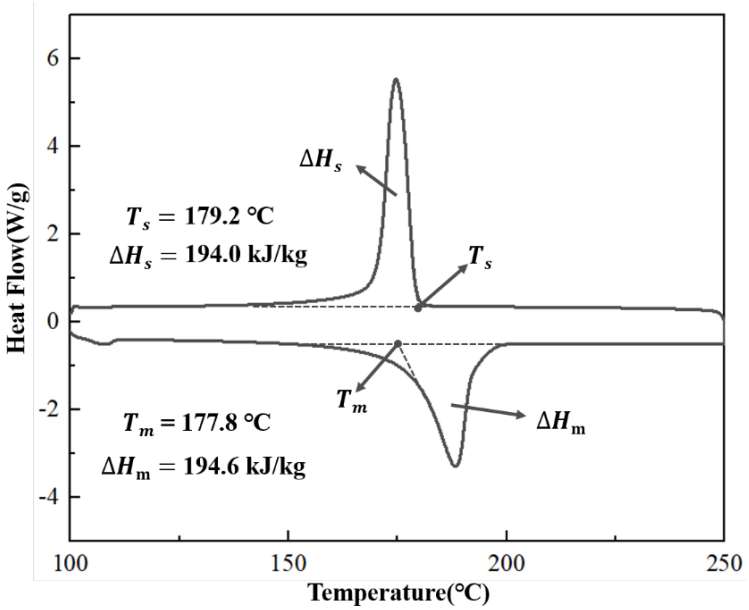

Fig. 8 DSC thermogram of LNK

Li et al [11] previously synthesized a molten salt with the same composition using the static melting method. Their results showed a melting point of 172.4 °C and a freezing point of 141.6 °C, accompanied by a large degree of supercooling (~30 °C). In contrast, the LNK prepared in this study via aqueous solution evaporation followed by drying exhibits negligible supercooling. Supercooling represents a metastable state where latent heat is not released until crystallization occurs, which is undesirable in practical TES applications due to its unpredictability and potential performance

degradation [45]. The DSC curves of the LNK obtained in this study show sharper melting and solidification peaks compared to those reported by Li et al [11], suggesting a more uniform phase change within a narrower temperature range. This indicates enhanced thermal homogeneity and crystallization behavior.

Yang et al [46] observed similar effects when adding NaCl in different forms (solid pellets vs. aqueous solution) to n-octadecane as a PCM. They found that the use of NaCl solution resulted in sharper DSC peaks and reduced supercooling. A dynamic Monte Carlo simulation [47] further revealed that during cooling, the dissolved ions can precipitate first, acting as nucleation sites that promote earlier crystallization and reduce supercooling. In analogy, the preparation methods used in this study, i.e., aqueous evaporation, can be considered as introducing KCl as a solution into the $LiNO_3$-$NaNO_3$ mixture. During cooling, the presence of dissolved species likely facilitates early nucleation, thereby improving crystallization kinetics and reducing supercooling.

3.6.2 Phase change behavior of NELNK

MTES plays a critical role in modulating the structure of the SiO_2 shell during nanocapsule synthesis. By adjusting the precursor ratio, MTES improves the flexibility and permeability of the silica network, the interfacial compatibility between the core and shell, and the encapsulation ratio [36]. To evaluate the phase change properties of both the pristine LNK and the NELNK, DSC was performed, and the resulting thermograms are shown in Fig. 9. In the DSC analysis, T_c and T_m represent the crystallization and melting temperatures, respectively. These values were determined by identifying the intersection of the extrapolated baseline with the tangent line drawn at the inflection point of the leading edge of each heat flow peak [48].

Since SiO_2 is thermally inert and does not undergo phase changes itself, the latent heat response of NELNK originates from the encapsulated LNK core material. Based on the measured enthalpies, the encapsulation ratio and encapsulation efficiency were calculated using the following equations:

$$R = (\Delta H_{\mathrm{m,NEPCM}}/\Delta H_{\mathrm{m,LNK}}) \times 100\% \quad (2)$$

$$E = (\Delta H_{\mathrm{m,NEPCM}} + \Delta H_{\mathrm{s,NEPCM}})/\left(\Delta H_{\mathrm{m,LNK}} + \Delta H_{\mathrm{s,LNK}}\right) \times 100\% \quad (3)$$

where $\Delta H_{\mathrm{m,NEPCM}}$ and $\Delta H_{\mathrm{s,NEPCM}}$ denote the melting and solidification enthalpies of the nanoencapsulated PCM, and $\Delta H_{\mathrm{m,LNK}}$ and $\Delta H_{\mathrm{s,LNK}}$ refer to those of the pure LNK, respectively.

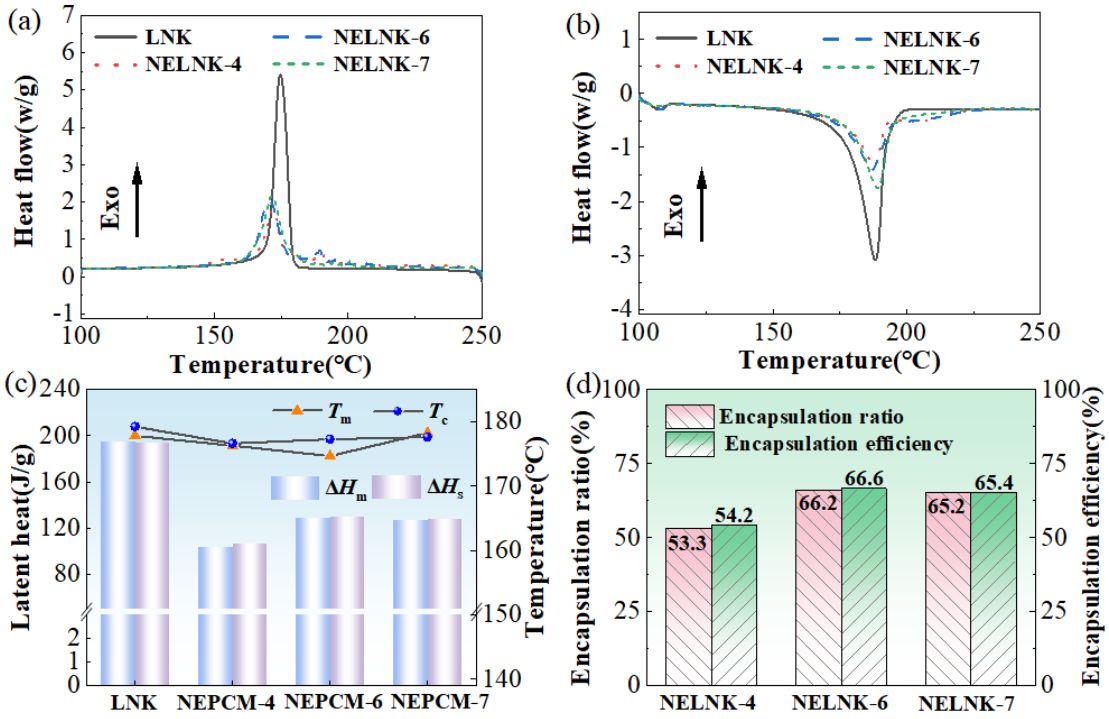

Fig. 9 Histograms of (a) solidification, (b) melting DSC curves, (c) latent heat and phase change temperature, (d) encapsulation ratio and encapsulation efficiency for LNK and NELNK

Analysis of the DSC curves (Fig. 9(a, b)) reveals that NELNK exhibits phase change peaks similar to those of LNK, with a single peak per cycle. This confirms that the encapsulation process is purely physical, without any chemical interaction between the core and the shell, which consistent with the FTIR and XRD analyses.

Further analysis (Fig. 9(c, d)) shows that the sample NELNK-6 achieves the highest phase change performance, with a melting enthalpy of 128.8 kJ/kg and an encapsulation ratio of 66.2%. This result highlights the importance of optimizing the precursor composition.

Notably, the melting and crystallization temperatures of NELNK are slightly lower than those of bulk LNK. This shift is attributed to the nanoscale confinement effect and weakened interfacial interactions between the core and shell materials. Similar findings have been reported in the literature: Mo et al. [25] observed a 2.9 °C reduction in

melting point for $LiNO_3$/NaCl@SiO_2 compared to the unencapsulated salt; Fang et al [49] also reported a decrease of 0.89–1.58 °C for paraffin microcapsules coated with SiO_2 shells. These phenomena suggest that the silica shell accelerates heat transfer to the core, initiating melting at a lower temperature, while simultaneously restricting molecular mobility, which delays crystallization.

To provide context for these findings, Table 3 summarizes studies on microencapsulated molten salts with SiO_2 shell, including their phase change temperatures, latent heats, encapsulation ratios, supercooling and particle sizes. Fig. 10 offers a three-dimensional visualization of the comparative data.

Table 3 Properties of NELNKs compared to previous studies

Sample	Melting point (℃)	Latent heat (kJ/kg)	Particle size (nm)	Encapsulation ratio (%)	ΔT(℃)	Ref.
$LiNO_3$+NaCl@SiO_2	222.4	228.7	741	66.20	8.0	[25]
Solar salt@SiO_2	225.9	66.9	886	60.19	8.8	[18]
Solar salt@GO/SiO_2	224.0	67.0	1363	60.32	8.9	[18]
Solar salt@SiO_2	225.3	107.8	41560	80.94	6.8	[19]
Solar salt@SiO_2	225.0	63.5	423	50.60	Na	[50]
Solar salt@SiO_2	224.9	88.5	614	61.60	9.8	[20]
Li_2CO_3+Na_2CO_3@SiO_2	498.0	220.7	5100	61.20	Na	[51]
$NaNO_3$@SiO_2	305.8	170.0	5000	89.00	Na	[52]
LNK@SiO_2	174.7	128.8	167	66.2	-2.7	Present

Note: “Na” represents that the data was not provided in the reference.

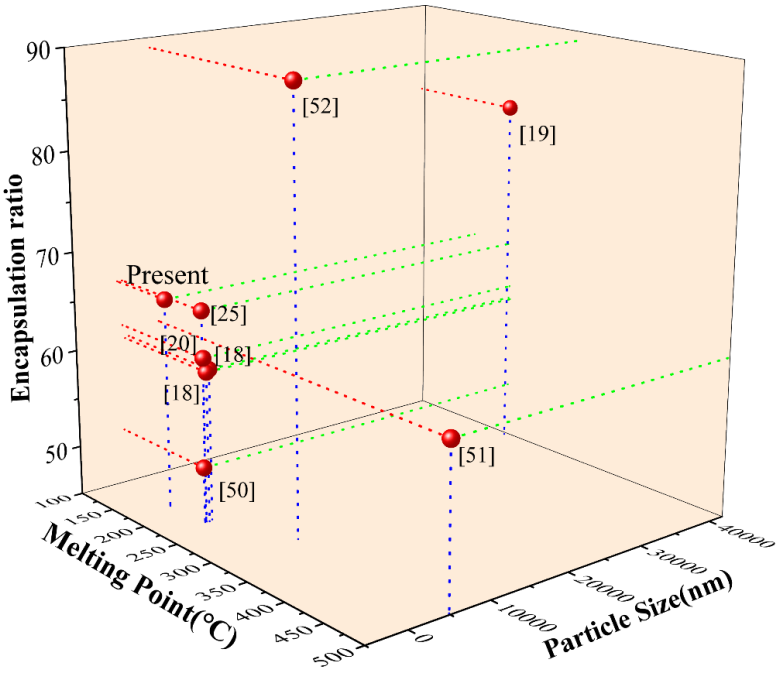

Fig. 10 Comparison between the present study and previous studies

Current microencapsulated molten salts commonly suffer from two major limitations: micrometer-scale particle sizes, and high phase change temperatures (>200 °C). Multicomponent eutectic salts face particular challenges, as their compositional balance is easily disrupted during encapsulation, often resulting in abnormal solidification behaviors such as bimodal phase change peaks. Single-component salts, by contrast, are easier to encapsulate, achieving encapsulation ratios exceeding 72% [41, 52]. Binary systems like Solar Salt typically exhibit poor eutectic stability, with encapsulation ratios rarely exceeding 60% [18, 20, 53]. Even with optimized techniques, the latent heat of binary salts remains around 107 kJ/kg [19]. For ternary molten salts, only a few studies report successful microencapsulation, with the highest encapsulation ratio reaching 63.7% [54]. These limitations restrict their applicability in medium-temperature solar TES systems. Moreover, larger particle sizes tend to reduce overall thermal storage capacity [55].

In contrast, this study demonstrates that by introducing MTES as a co-precursor and optimizing the precursor ratio, it is possible to achieve nanoscale particle size while maintaining eutectic composition and avoiding bimodal solidification. As a result, the encapsulation ratio of the ternary LNK reaches 66.2% , surpassing previously reported

values. The corresponding phase change enthalpy is 128.8 kJ/kg , which is 1.2 times higher than that of Solar Salt, and the melting point is reduced by 50 °C, making it the lowest among current molten salt nanocapsules.

The degree of supercooling is defined as the temperature difference between the melting point and the crystallization (solidification) point and can be expressed by the following equation:

$$\Delta T = T_m - T_s \quad (4)$$

where ΔT denotes the degree of supercooling, T_m is the melting temperature, and T_s is the solidification (crystallization) temperature. In this study, the degree of supercooling is calculated using Equation (4). Notably, LNK@SiO_2 exhibits a negative degree of supercooling. This occurs because both the melting and solidification temperatures are defined as the onset temperatures, i.e., the points where the baseline intersects the melting or solidification peak in the heat flow curve [56] (see Fig. 8). The onset temperature was selected as the phase change temperature because it is less sensitive to variations in sample mass and heating/cooling rates. Negative supercooling values have also been reported in the literature [45, 57]. The SiO_2 shell functions as a nucleating agent [19], providing heterogeneous nucleation sites that significantly suppress supercooling in LNK@SiO_2. This reduction in supercooling enhances the material's suitability for TES applications.

As evident from Table 3, previously reported molten salt phase change microcapsules typically exhibit significant supercooling, a persistent challenge that compromises TES performance. In contrast, the suppression of supercooling achieved in this study represents a substantial advancement, offering distinct advantages for real-world TES applications where consistent and predictable phase change behavior is critical. This breakthrough highlighting its potential for medium-temperature applications (100–200 °C), particularly in medium-temperature solar TES.

Based on the combined morphological and thermal property analyses, NELNK-6 demonstrates superior structural integrity and thermal performance. Therefore, subsequent experimental investigations and discussions will focus on this sample.

3.7 Thermal reliability analysis of NELNK

In practical TES applications, microencapsulated PCMs must maintain good thermal performance over repeated heating–cooling cycles. Fig. 11 compares the macroscopic morphologies of LNK and NELNK after undergoing phase changes. The pure LNK sample exhibits strong adhesion during melting and solidifies into a waxy mass that firmly adheres to the container walls, making it difficult to remove. In contrast, the NELNK remain in a loose powder form after the same process, indicating that the SiO_2 shell effectively isolates the LNK core from the external environment, preventing leakage and significantly enhancing both stability and practical applicability.

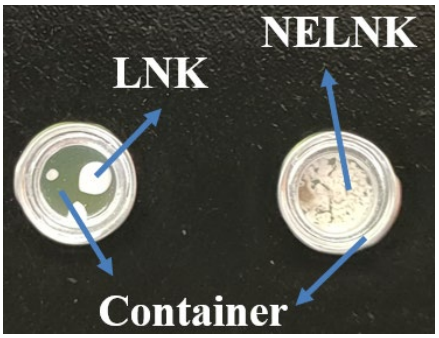

Fig. 11 Appearance of LNK and NELNK after DSC test

To evaluate the long-term thermal cycling stability of NELNK-6, 100 consecutive heating–cooling cycles were conducted. Each cycle consisted of heating the sample from 30 °C to 190 °C at a rate of 10 °C/min, holding at 190 °C for 5 min to ensure complete melting, followed by natural cooling to room temperature. After every 20 thermal cycles, samples were randomly selected for post-cycling characterization.

As shown in Fig. 12(a), SEM analysis confirmed that the NELNK nanocapsules retained their well-defined spherical morphology throughout cycling, with no observable rupture, aggregation, or structural deformation. Furthermore, FTIR spectra recorded before and after 100 cycles (Fig. 12(b)) exhibited no discernible peak shifts or intensity variations in characteristic absorption bands, indicating the absence of chemical interaction between the core and shell materials and confirming chemical stability over repeated thermal stress.

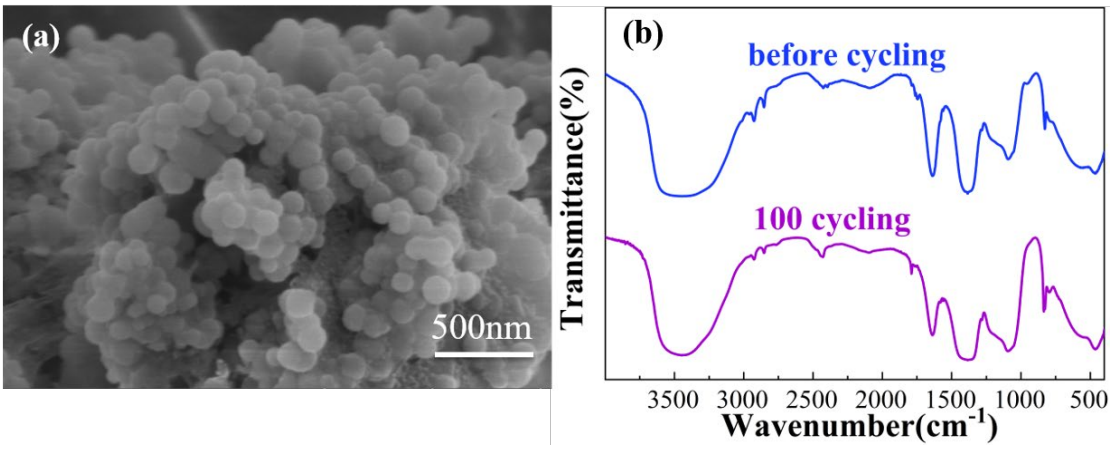

Fig. 12 (a) SEM and (b) FTIR plots of NELNK after 100 thermal cycles

Collectively, these results demonstrate that the silica shell effectively encapsulates and confines the molten salt core, preserving structural, morphological, and chemical integrity across extended thermal cycling.

The resulting DSC thermograms are shown in Fig. 13, with corresponding data summarized in Table 4. To quantitatively assess thermal reliability, the energy storage efficiency (E_{SE}) was introduced as an evaluation index, calculated using the following equation:

$$E_{SE} = (\Delta H_m + \Delta H_s)_{\text{after cycling}} / (\Delta H_m + \Delta H_s)_{\text{before cycling}} \quad (5)$$

where $\Delta H_{\text{before cycling}}$ and $\Delta H_{\text{after cycling}}$ denote the latent heat of phase change before and after cycling. The results are also listed in Table 4.

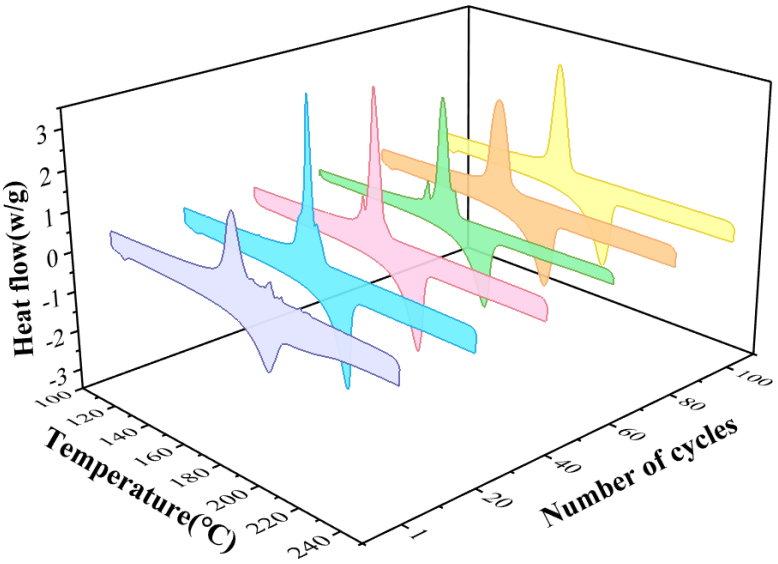

Fig. 13 DSC thermograms of NELNK acquired after thermal cycles

Table 4 DSC data of NELNK after thermal cycles

Cycle number	T_m (°C)	T_s (°C)	ΔH_m (kJ/kg)	ΔH_s (kJ/kg)	E_{SE} (%)
1	174.6	177.3	128.8	130.0	100.0
20	179.6	173.6	130.6	128.7	100.2
40	179.0	172.7	131.3	129.6	100.8
60	177.3	172.4	127.3	127.0	98.3
80	177.6	171.9	129.2	129.0	99.8
100	178.2	172.1	126.8	128.0	98.5

Fig. 13 presents the DSC curves and trends in phase change temperature and latent heat of NELNK-6 after different numbers of thermal cycles. The melting peak position and height remain nearly unchanged after 100 cycles, indicating excellent reproducibility in phase change behavior. As shown in Table 4, the phase change temperature exhibits only minor fluctuations, likely due to cumulative structural distortions in the eutectic salt during repeated melting and solidification [42].

As summarized in Table 4, the latent heat of phase change exhibits exceptional stability, with only minimal variation observed during the first 40 thermal cycles. The E_{SE} remained high at 98.3% after 60 cycles and even slightly increased to 99.8% after 80 cycles. This minor fluctuation is negligible and can be attributed to experimental uncertainty inherent in DSC measurements, a phenomenon also reported in other studies [58]. Critically, FTIR analysis revealed no evidence of chemical degradation in the PCM throughout the cycling tests, confirming that the observed enthalpy variations are of physical rather than chemical origin. Consequently, these small changes in latent heat are deemed insignificant and well within the acceptable range for practical TES applications. After 100 cycles, the E_{SE} showed a value of 98.5% which is close to that after 60 cycles, confirming the great long-term reliability of NELNK.

Specifically, the latent heats of melting and solidification decrease by only 2.0 kJ/kg, less than 2.0%. This indicates that the phase change properties remain largely unaffected, maintaining high energy storage capacity. This superior performance is primarily attributed to the dense encapsulation provided by the Si–O–Si three-dimensional network in the SiO_2 shell, which effectively prevents core leakage.

Additionally, the introduction of alkyl groups via MTES enhances the mechanical toughness of the shell, improving resistance to breakage during thermal cycling and reducing performance degradation. Some minor fluctuations in enthalpy may also arise from measurement uncertainty.

In summary, the NELNK demonstrate great thermal reliability after repeated phase changes. To further contextualize this result, Table 5 compares the energy storage efficiency of NELNK-6 with previously reported silica-coated microcapsules. Notably, NELNK-6 outperforms existing results, especially within the ternary molten salt category, demonstrating superior thermal cycling stability and energy storage efficiency.

Table 5 Thermal reliability of NELNK compared to previous studies

Micro/nanocapsules	Number of cycles	E_{SE} (%)	Ref
D-mannitol@SiO_2	50	68.8	[42]
GA@SiO_2	50	97.4	[59]
Erythritol@SiO_2	60	82.2	[60]
$Na_2SO_4 \cdot 10H_2O$@SiO_2	100	79.9	[61]
$LiNO_3$@SiO_2	10	96.5[a]	[41]
$NaNO_3$+MXene@SiO_2	50	94.6	[62]
$Na_2HPO_4 \cdot 12H_2O$+ MXene@SiO_2	50	83.6[a]	[63]
K_2CO_3+Li_2CO_3@SiO_2	100	97.4	[64]
K_2CO_3/Li_2CO_3/Na_2CO_3@SiO_2	50	80.7	[54]
$LiNO_3$+ $NaNO_3$+KCl@SiO_2	100	98.5	Present

Note: [a] Value calculated from data in the literature

3.8 Thermal stability analysis of NELNK

Thermal stability is a critical parameter for evaluating the durability of microencapsulated PCMs under working-temperature conditions. In this study, the thermal decomposition behavior of both pristine LNK and NELNK-6 was analyzed using TGA, with the resulting curves presented in Fig. 14. Key thermal events are annotated directly on the curves. The decomposition onset temperature was determined using the extrapolated initial mass loss method, defined as the point where significant weight loss begins on the TGA curve [65], and is indicated in blue on the figure.

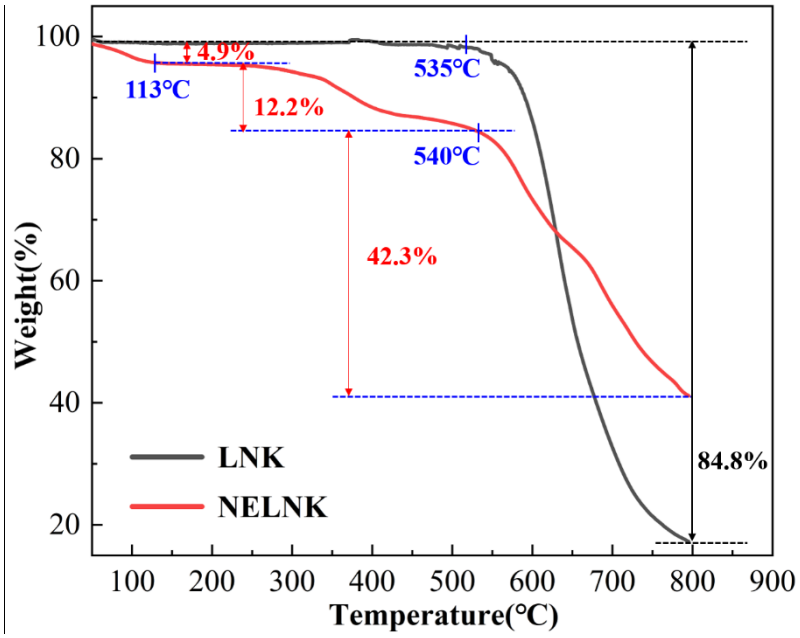

Fig. 14 TGA curves of LNK and NELNK, highlighting decomposition temperatures and degradation stages

The TGA profile of pristine LNK exhibits a single-step weight loss, with the material remaining stable between room temperature and approximately 535 °C. Significant decomposition begins above this temperature and is primarily attributed to the thermal degradation of $LiNO_3$ and $NaNO_3$, resulting in a mass loss of approximately 84.8%. This decomposition is consistent with the following reactions:

$$4LiNO_3 \rightarrow 2Li_2O + 4NO_2 + O_2 \quad (6)$$

$$2NaNO_3 \rightarrow 2NaNO_2 + O_2 \quad (7)$$

$$4NaNO_2 \rightarrow 2Na_2O + 4NO + O_2 \quad (8)$$

In contrast, NELNK exhibits a more complex, three-stage weight loss profile, reflecting the influence of the SiO_2 shell on heat transfer and thermal degradation dynamics:

First Stage (room temperature–113 °C): A minor weight loss of approximately 4.9% occurs, primarily due to the evaporation of residual physically adsorbed moisture on the surface of the nanocapsules, which was absorbed from ambient air during handling and storage.

Second Stage (113–540 °C): A moderate weight loss of ~12.2% is observed, mainly caused by the dehydration and condensation of residual silanol groups (Si–OH)

in the SiO_2 shell formed during synthesis [66]. Additionally, decomposition of residual surfactants used in the encapsulation process likely contributes to mass loss in this temperature range. This interpretation is supported by prior studies showing that surfactant-free microcapsules exhibit significantly reduced weight loss during this stage [67].

Third Stage (>540 °C): This stage corresponds to the main decomposition event, involving the thermal breakdown of $LiNO_3$ and $NaNO_3$ into metal oxides and gaseous byproducts, resulting in a cumulative mass loss of 42.3%. Notably, the decomposition rate of NELNK is considerably slower than that of unencapsulated LNK. This retardation is attributed to the protective barrier by the dense SiO_2 shell at high temperatures, which inhibits gas diffusion and retards the decomposition of the core material. This behavior further confirms the structural integrity and effective encapsulation achieved in NELNK.

In summary, NELNK exhibits a typical three-stage thermal decomposition profile commonly observed in silica-coated microcapsules [33, 55, 68, 69]. Importantly, no significant mass loss occurs below 540 °C except for trace contributions from unreacted silica precursors, indicating high thermal stability across the operational temperature range (room temperature to 540 °C). Moreover, previous studies have demonstrated that SiO_2 shells prepared with MTES maintain good hydrophobicity up to 420 °C [31], further enhancing the moisture resistance and long-term reliability of NELNK in high-temperature environments.

3.9 Moisture resistance performance analysis of NELNK

To systematically evaluate the moisture resistance of both the pristine LNK eutectic salt and NELNK, samples were exposed to environments with varying RH, and their hygroscopic behaviors were quantitatively analyzed by monitoring mass changes over time. This analysis provides insight into the material's long-term stability under real-world storage and operational conditions.

The moisture absorption rate was calculated using the following equation:

$$M_r = (m_t - m_0)/m_0 \times 100\% \quad (9)$$

where m_0 is the initial mass of the sample, and m_t is the mass after exposure to a specific RH environment for a given time t. During the experiment, samples were placed in controlled humidity chambers at 40%, 60%, and 80% RH for a duration of 24 h. Mass measurements were taken at regular intervals, and the results were plotted as moisture absorption rate versus time, as shown in Fig. 15.

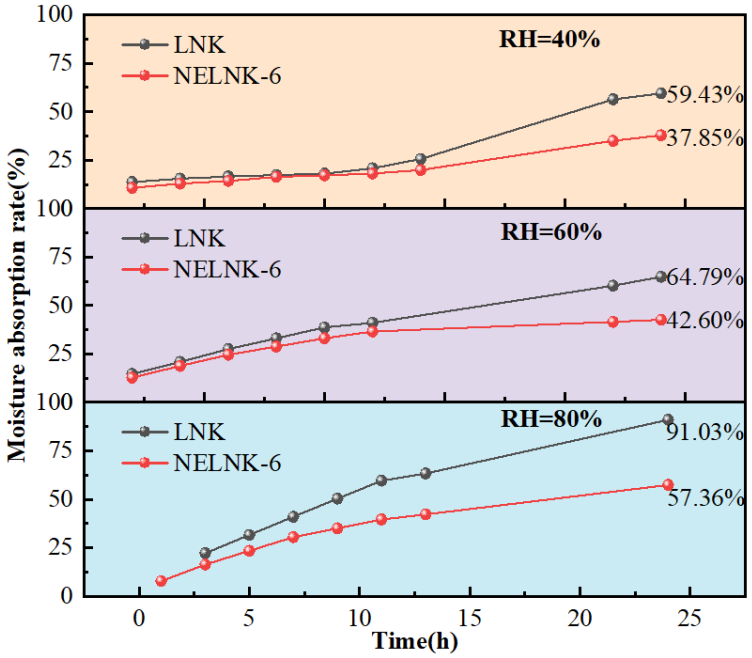

Fig. 15 Variation of moisture absorption of LNK and NELNK with time

The experimental results indicate that both LNK and NELNK exhibit increased moisture absorption with rising ambient humidity; however, their sensitivity to environmental moisture differs significantly. Notably, the moisture absorption rate of NELNK is substantially lower than that of pure LNK, demonstrating superior moisture resistance.

This enhanced performance can be attributed to the presence of a dense SiO_2 shell, which acts as an effective physical barrier that prevents moisture from penetrating and contacting with the hygroscopic LNK core. This mechanism aligns with findings reported by Mo et al. [25].

To further elucidate the relationship between moisture resistance and surface wettability, contact angle measurements were conducted on MTES-modified SiO_2 surface in accordance with ASTM D7334, using a water droplet volume of 2 μL. The contact angle was recorded immediately after water droplet deposition, with the

reported value representing the average of three independent measurements. As illustrated in Fig. 16, the measured contact angle of 98° confirms the hydrophobic nature of the surface, demonstrating that MTES incorporation effectively enhances the water repellency of the silica shell.

This hydrophobic behavior arises from the integration of methyl ($–CH_3$) groups into the Si–O–Si network during hydrolysis and condensation of MTES. These hydrophobic moieties partially substitute hydrophilic surface silanol (–Si–OH) groups, thereby imparting hydrophobicity and enhanced moisture resistance to the nanocapsules.

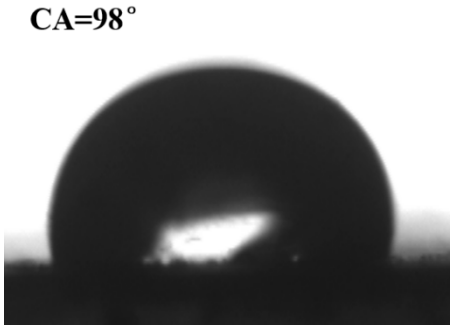

Fig. 16 Contact angle of NELNK

Although moisture resistance is critical to the long-term performance and real-world applicability of molten salt PCMs, studies quantifying moisture absorption remain relatively scarce. Prolonged exposure to humid conditions can severely compromise material performance through moisture-induced degradation. To provide a broader context, Table 6 summarizes available data on the moisture resistance of various PCMs reported in the literature.

Table 6. Reduction in moisture absorption rate of molten salt composites after exposure to varying humidity conditions.

PCM composites	RH (%)	Reduction in moisture absorption rate (%)[b]	Ref
Na_2CO_3-K_2CO_3/MgO/glass	80	11.15[a]	[22]
$LiNO_3$+NaCl@SiO_2	46–51	0.6[a]	[25]
$LiNO_3$+NaCl@SiO_2	67–72	8[a]	[25]
$LiNO_3$+NaCl@SiO_2	84–87	9.6[a]	[25]

NELNK	40	21.58	This study
NELNK	60	22.19	This study
NELNK	80	33.67	This study

Note: [a] Value calculated from data in the literature.

[b] "Reduction in moisture absorption (%)" represents a decrease in absolute moisture absorption rate.

Notably, the hygroscopic behavior of molten salts varies considerably across different PCMs. For instance, Lu et al. [22] reduced the moisture absorption of a hygroscopic Na_2CO_3–K_2CO_3/MgO composite from 15.25% to 4.10% by incorporating silicate glass. In comparison, the NELNK developed in this study demonstrate significantly improved moisture resistance. Mo et al. [25] reported that $LiNO_3$/NaCl@SiO_2 microcapsules synthesized using TEOS as the sole silica precursor exhibited moisture absorption reductions of 0.6%, 8%, and 9.6% under RH levels of 46–51%, 67–72%, and 84–87%, respectively. Remarkably, NELNK outperforms these results, achieving reductions of 21.58%, 22.19%, and 33.67% under comparable humidity conditions, underscoring its exceptional environmental resilience.

The superior moisture resistance of NELNK stems from two synergistic effects enabled by MTES modification:

(1) The silica shell, as confirmed by TEM and SEM analyses, forms a continuous, dense physical barrier that effectively impedes water molecule penetration.

(2) Hydrophobic methyl (–CH_3) groups, incorporated into the silica network via hydrolysis and condensation of MTES during shell formation, significantly reduce surface hydrophilicity. This observation is consistent with the work of Dudas et al. [30], who demonstrated that MTES incorporation can tune surface wettability, even inducing a transition from hydrophilic to hydrophobic behavior.

In summary, the NELNK nanocapsules synthesized in this study exhibit dramatically enhanced moisture resistance. The MTES-mediated modification strategy not only retards moisture absorption but also substantially improves long-term durability under humid conditions. As such, this approach represents a robust pathway

to mitigate moisture-induced degradation in highly hygroscopic molten salt systems.

4 Conclusions

This study aimed to address challenges faced by molten salt PCMs, including leakage, poor thermal stability, and hygroscopicity. A novel strategy was developed to overcome these limitations by incorporating MTES to form a flexible, moisture-resistant silica shell for encapsulating hygroscopic molten salts. The resulting NELNK nanocapsules exhibited excellent phase change performance, with a melting temperature of 174.7 °C, a latent heat of 128.8 kJ/kg, along with an encapsulation ratio of 66.2%.The NELNK nanocapsules demonstrated outstanding thermal reliability, retaining 98.3% of their initial energy storage efficiency after 50 thermal cycles. Moreover, the incorporation of MTES significantly enhanced moisture resistance, reducing the moisture absorption rate by 21.58–33.67% under various humidity levels from 40% to 80% RH compared to the unencapsulated LNK. By introducing MTES and optimizing the composition of the precursors, this work effectively improved the encapsulation ratio and overall performance of ternary molten salts. The improvements increase the application potential of molten salts in medium-temperature TES systems and the feasibility of application in humid environments.

Building on these findings, we outline key future research directions to advance this technology toward practical deployment. First, from a manufacturing standpoint, replacing the current emulsification system with more cost-effective alternatives will be essential to improve process economics, without compromising encapsulation ratio or shell integrity. Second, to bridge the gap between material innovation and system-level integration, future work will prioritize the quantitative assessment of nanocapsule packing density. This critical parameter will enable accurate calculation of volumetric energy density, a decisive metric for evaluating performance in real-world TES systems. Third, dynamic thermal-humidity cycling would provide a more operationally relevant simulation of concentrating solar power system environments. Such testing is critical for validating real-world performance, and future studies must incorporate dynamic

thermal-humidity cycling to rigorously assess long-term durability under conditions that accurately replicate operational stresses in CSP systems.

Credit authorship contribution statement

Qing Li: Investigation, Writing-original draft. Songping Mo: Conceptualization, Funding acquisition, Methodology, Project administration, Supervision, Writing-review & editing. Yuxuan Lin: Investigation. Lisi Jia: Writing-review & editing. Zhi Yang: Writing-review & editing. Yanping Du: Writing-review & editing. Ying Chen: Resources.

Declaration of competing interest

The authors declare that they have no known competing financial interests or personal relationships that could have appeared to influence this work.

Data availability

Data will be made available on request.

Acknowledgements

This work was supported by the National Natural Science Foundation of China [grant number 51976040].

References

[1] Hamzat, A. K.; Pasanaje, A. H.; Omisanya, M. I.; Sahin, A. Z.; Maselugbo, A. O.; Adediran, I. A.; Mudashiru, L. O.; Asmatulu, E.; Oyetunji, O. R.; Asmatulu, R., Phase change materials in solar energy storage: Recent progress, environmental impact, challenges, and perspectives. *Journal of Energy Storage* **2025,** *114*, 115762.https://doi.org/10.1016/j.est.2025.115762.

[2] Mo, S.; Li, J.; Lin, Y.; Yang, Z.; Wang, Z.; Jia, L.; Du, Y.; Chen, Y., Nanoencapsulation and performance of water-insoluble sebacic acid as a phase change material for medium-temperature thermal energy storage. *Applied Thermal Engineering* **2025,** *277*, 126975.https://doi.org/10.1016/j.applthermaleng.2025.126975.

[3] Ali, S.; Deshmukh, S. P., An overview: Applications of thermal energy storage using phase change materials. *Materials Today: Proceedings* **2020,** *26*, 1231-1237.https://doi.org/10.1016/j.matpr.2020.02.247.

[4] Lin, W.; Zeng, J.; Liang, C.; Cheng, J.; Wang, Y.; Qu, W.; Li, C.; Guan, Y.; Li, S., The synthesis and characterization of phase change material microcapsules with titanium oxide nanotubes for thermal energy regulation. *Applied Thermal Engineering* **2024,** *236*, 121703.https://doi.org/10.1016/j.applthermaleng.2023.121703.

[5] Zhang, H.; Zhang, X.; Pan, D.; Ai, Y.; Chen, Y., Preparation and application of high-temperature composite phase change materials. *Journal of Energy Storage* **2023,** *68*, 107669.https://doi.org/10.1016/j.est.2023.107669.
[6] Sikiru, S.; Oladosu, T. L.; Amosa, T. I.; Kolawole, S. Y.; Soleimani, H., Recent advances and impact of phase change materials on solar energy: A comprehensive review. *Journal of Energy Storage* **2022,** *53*, 105200.https://doi.org/10.1016/j.est.2022.105200.
[7] Zhang, H.; Xu, C.; Fang, G., Encapsulation of inorganic phase change thermal storage materials and its effect on thermophysical properties: A review. *Solar Energy Materials and Solar Cells* **2022,** *241*, 111747.https://doi.org/10.1016/j.solmat.2022.111747.
[8] Bhatnagar, P.; Siddiqui, S.; Sreedhar, I.; Parameshwaran, R., Molten salts: Potential candidates for thermal energy storage applications. *International Journal of Energy Research* **2022,** *46* (13), 17755-17785.https://doi.org/10.1002/er.8441.
[9] Fang, M.; Cao, L.; Cao, Y.; Hou, F., Enhanced thermal energy storage in molten salt-based date-occupied composites with SiO_2 nanoparticles. *Applied Thermal Engineering* **2025,** *270*, 126209.https://doi.org/10.1016/j.applthermaleng.2025.126209.
[10] Kenisarin, M. M., High-temperature phase change materials for thermal energy storage. *Renewable and Sustainable Energy Reviews* **2010,** *14* (3), 955-970.https://doi.org/10.1016/j.rser.2009.11.011.
[11] Li, Y.; Yue, G.; Yu, Y. M.; Zhu, Q. Z., Preparation and thermal characterization of $LiNO_3$–$NaNO_3$–KCl ternary mixture and $LiNO_3$–$NaNO_3$–KCl/EG composites. *Energy* **2020,** *196*, 117067.https://doi.org/10.1016/j.energy.2020.117067.
[12] Sang, L.; Lv, X.; Wu, Y., $NaNO_3$-KNO_3-KCl/K_2CO_3 with the elevated working temperature for CSP application: Phase diagram calculation and machine learning. *Sol Energy* **2023,** *252*, 322-329.https://doi.org/10.1016/j.solener.2023.02.009.
[13] Chen, X.; Gao, H.; Tang, Z.; Dong, W.; Li, A.; Wang, G., Optimization strategies of composite phase change materials for thermal energy storage, transfer, conversion and utilization. *Energy & Environmental Science* **2020,** *13* (12), 4498-4535.https://doi.org/10.1039/d0ee01355b.
[14] Huang, Y.; Stonehouse, A.; Abeykoon, C., Encapsulation methods for phase change materials – A critical review. *Int J Heat Mass Tran* **2023,** *200*, 123458.https://doi.org/10.1016/j.ijheatmasstransfer.2022.123458.
[15] Zhang, H.; Balram, A.; Tiznobaik, H.; Shin, D.; Santhanagopalan, S., Microencapsulation of molten salt in stable silica shell via a water-limited sol-gel process for high temperature thermal energy storage. *Applied Thermal Engineering* **2018,** *136*, 268-274.https://doi.org/10.1016/j.applthermaleng.2018.02.050.
[16] Park, S.; Jo, B., Novel surfactant-free microencapsulation of molten salt using TiO_2 shell for high temperature thermal energy storage: Thermal performance and thermal reliability. *Journal of Energy Storage* **2023,** *63*, 107016.https://doi.org/10.1016/j.est.2023.107016.
[17] Lee, J.; Jo, B., Surfactant-free synthesis protocol of robust and sustainable molten salt microcapsules for solar thermal energy storage. *Solar Energy Materials and Solar Cells* **2021,** *222*, 110954.https://doi.org/10.1016/j.solmat.2020.110954.
[18] Ji, W.; Cheng, X.; Chen, H.; Li, L.; Li, Y.; Liu, Z., Efficient synthesis of regular spherical GO/SiO_2@Solar Salt microcapsules to enhance heat-storage capacity and cycle stability. *Energy Conversion and Management* **2021,** *245*, 114637.https://doi.org/10.1016/j.enconman.2021.114637.
[19] Pethurajan, V.; Suresh, S.; Mojiri, A.; Konatt, A. J., Microencapsulation of nitrate salt for solar

thermal energy storage- synthesis, characterisation and heat transfer study. *Solar Energy Materials and Solar Cells* **2020,** *206*, 110308.https://doi.org/10.1016/j.solmat.2019.110308.
[20] Wang, L.; Huang, Y.; Li, L.; Li, Y.; Cheng, X., Binary nitrate molten salt magnetic microcapsules modified with Fe3O4-functionalized carbon nanotubes for accelerating thermal energy storage. *Journal of Energy Storage* **2023,** *74*, 109394.https://doi.org/10.1016/j.est.2023.109394.
[21] Guo, P. F.; Qiu, Z. S.; Zhang, Y. B.; Zhong, H. Y.; Zhao, X.; Zang, X. Y.; Wang, D.; Shan, K., Preparation and characterization of phase change microcapsules for improving the applicable temperature and stability of high temperature resistant drilling fluids. *Chem Eng Res Des* **2024,** *201*, 389-398.http://doi.org/10.1016/j.cherd.2023.11.054.
[22] Lu, Y. K.; Zhang, G. Q.; Hao, J. J.; Ren, Z. K.; Deng, Z. F.; Xu, G. Z.; Yang, C. Y.; Chang, L., Fabrication and characterization of the novel shape-stabilized composite PCMs of Na_2CO_3-K_2CO_3/MgO/glass. *Sol Energy* **2019,** *189*, 228-234.https://doi.org/10.1016/j.solener.2019.07.064.
[23] Cabeza, L. F.; Martínez, F. R.; Borri, E.; Ushak, S.; Prieto, C. Thermal Energy Storage Using Phase Change Materials in High-Temperature Industrial Applications: Multi-Criteria Selection of the Adequate Material *Materials* [Online], 2024.
[24] Deng, Z. F.; Liu, Z. H.; Zhang, G. Q.; Xu, G. Z.; Yang, C. Y., Effect of humidity environment on properties of molten salt phase change materials. *IOP Conference Series: Materials Science and Engineering* **2019,** *504* (504), 012010.https://doi.org/10.1088/1757-899x/504/1/012010.
[25] Mo, S. P.; Xiao, B.; Li, J. X.; Jia, L. S.; Chen, Y., $LiNO_3$/NaCl nanocapsules with high thermal properties for medium-temperature thermal energy storage. *Journal of Energy Storage* **2024,** *83*, 110672.https://doi.org/10.1016/j.est.2024.110672.
[26] Zhu, C.; Lin, Y.; Fang, G., Preparation and thermal properties of microencapsulated stearyl alcohol with silicon dioxide shell as thermal energy storage materials. *Applied Thermal Engineering* **2020,** *169*, 114943.https://doi.org/10.1016/j.applthermaleng.2020.114943.
[27] Pisal, A. A.; Rao, A. V., Comparative studies on the physical properties of TEOS, TMOS and Na_2SiO_3 based silica aerogels by ambient pressure drying method. *Journal of Porous Materials* **2016,** *23* (6), 1547-1556.https://doi.org/10.1007/s10934-016-0215-y.
[28] Darmawan, A.; Handayani, D. L.; Saputra, R. E., Hydrophobic silica films derived from methyltriethoxysilane (MTES): Effect of pH and calcination temperature. *Applied Physics A* **2021,** *127* (9), 649.https://doi.org/10.1007/s00339-021-04794-1.
[29] Liu, Q.; Kong, Y.; Shen, X. D., Regulating the hydrophobicity and pore structure of silica aerogel for thermal insulation under humid and high temperature conditions. *Journal of Porous Materials* **2025,** *32* (1), 171-180.https://doi.org/10.1007/s10934-024-01691-9.
[30] Dudás, Z.; Len, A.; Ianăși, C.; Paladini, G., Structural modifications caused by the increasing MTES amount in hybrid MTES/TEOS-based silica xerogels. *Mater Charact* **2020,** *167*, 110519.https://doi.org/10.1016/j.matchar.2020.110519.
[31] Darmawan, A.; Munzakka, L.; Karlina, L.; Saputra, R. E.; Sriatun, S.; Astuti, Y.; Wahyuni, A. S., Pervaporation membrane for desalination derived from tetraethylorthosilicate-methyltriethoxysilane. *Journal of Sol-Gel Science and Technology* **2022,** *101* (3), 505-518.https://doi.org/10.1007/s10971-022-05754-8.
[32] Fei, X.; Liu, S.; Zhang, B.; Zhao, H., Effect of alkyltriethoxysilane on the performance of sodium silicate-based silica shell phase change microcapsules. *Colloids and Surfaces A: Physicochemical and Engineering Aspects* **2021,** *608*, 125503.https://doi.org/10.1016/j.colsurfa.2020.125503.

[33] Lin, Y.; Zhu, C.; Fang, G., Synthesis and properties of microencapsulated stearic acid/silica composites with graphene oxide for improving thermal conductivity as novel solar thermal storage materials. *Solar Energy Materials and Solar Cells* **2019,** *189*, 197-205.https://doi.org/10.1016/j.solmat.2018.10.005.
[34] Alva, G.; Huang, X.; Liu, L.; Fang, G., Synthesis and characterization of microencapsulated myristic acid–palmitic acid eutectic mixture as phase change material for thermal energy storage. *Applied Energy* **2017,** *203*, 677-685.https://doi.org/10.1016/j.apenergy.2017.06.082.
[35] Zhang, H.; Wang, X.; Wu, D., Silica encapsulation of n-octadecane via sol–gel process: A novel microencapsulated phase-change material with enhanced thermal conductivity and performance. *Journal of Colloid and Interface Science* **2010,** *343* (1), 246-255.https://doi.org/10.1016/j.jcis.2009.11.036.
[36] Zhang, B.; Zhu, Y.; Yuan, Y.; Fang, Q.; Zhao, H., Preparation and performance evaluation of paraffin@SiO_2 microencapsulated phase change material and its thermal insulation effect in architectural coatings. *Colloids and Surfaces A: Physicochemical and Engineering Aspects* **2025,** *722*, 137287.https://doi.org/10.1016/j.colsurfa.2025.137287.
[37] Seraji, M. M.; Sameri, G.; Davarpanah, J.; Bahramian, A. R., The effect of high temperature sol-gel polymerization parameters on the microstructure and properties of hydrophobic phenol-formaldehyde/silica hybrid aerogels. *Journal of Colloid and Interface Science* **2017,** *493*, 103-110.https://doi.org/10.1016/j.jcis.2017.01.014.
[38] Tang, F.; Liu, L.; Alva, G.; Jia, Y.; Fang, G., Synthesis and properties of microencapsulated octadecane with silica shell as shape–stabilized thermal energy storage materials. *Solar Energy Materials and Solar Cells* **2017,** *160*, 1-6.https://doi.org/10.1016/j.solmat.2016.10.014.
[39] San Vicente, G.; Bayón, R.; Germán, N.; Morales, A., Surface modification of porous antireflective coatings for solar glass covers. *Sol Energy* **2011,** *85* (4), 676-680.https://doi.org/10.1016/j.solener.2010.06.009.
[40] Sulaiman, M.; Rahman, A. A.; Mohamed, N. S., Effect of water-based sol gel method on structural, thermal and conductivity properties of LiNO3–Al2O3 composite solid electrolytes. *Arab. J. Chem.* **2017,** *10* (8), 1147-1152.https://doi.org/10.1016/j.arabjc.2015.04.031.
[41] Mo, B.; Mo, S.; Jia, L.; Wang, Z.; Chen, Y., Microencapsulation of ethanol-soluble inorganic salts for high temperature thermal energy storage. *Materials Chemistry and Physics* **2022,** *275*, 125261.https://doi.org/10.1016/j.matchemphys.2021.125261.
[42] He, L.; Mo, S.; Lin, P.; Jia, L.; Chen, Y.; Cheng, Z., Synthesis and properties of nanoencapsulated D-mannitol for medium temperature thermal energy storage. *Solar Energy Materials and Solar Cells* **2020,** *209*, 110473.https://doi.org/10.1016/j.solmat.2020.110473.
[43] Fang, Y.; Huang, L.; Liang, X.; Wang, S.; Wei, H.; Gao, X.; Zhang, Z., Facilitated synthesis and thermal performances of novel SiO_2 coating $Na_2HPO_4{\cdot}7H_2O$ microcapsule as phase change material for thermal energy storage. *Solar Energy Materials and Solar Cells* **2020,** *206*, 110257.https://doi.org/10.1016/j.solmat.2019.110257.
[44] Sato, H.; Kataoka, N.; Kajiya, F.; Katano, M.; Takigawa, T.; Masuda, T., Kinetic study on the elastic change of vascular endothelial cells on collagen matrices by atomic force microscopy. *Colloids and Surfaces B: Biointerfaces* **2004,** *34* (2), 141-146.https://doi.org/10.1016/j.colsurfb.2003.12.013.
[45] Zahir, M. H.; Mohamed, S. A.; Saidur, R.; Al-Sulaiman, F. A., Supercooling of phase-change materials and the techniques used to mitigate the phenomenon. *Applied Energy* **2019,** *240*, 793-

817.10.1016/j.apenergy.2019.02.045.
[46] Yang, Y.; Luo, J.; Li, S.; Song, G.; Liu, Y.; Tang, G., The experimental exploration of sodium chloride solution on thermal behavior of phase change materials. *Solar Energy Materials and Solar Cells* **2015,** *139*, 88-94.https://doi.org/10.1016/j.solmat.2015.03.009.
[47] Hu, W.; Frenkel, D., Effect of Metastable Liquid−Liquid Demixing on the Morphology of Nucleated Polymer Crystals. *Macromolecules* **2004,** *37* (12), 4336-4338.https://doi.org/10.1021/ma049581t.
[48] Rady, M., Study of phase changing characteristics of granular composites using differential scanning calorimetry. *Energy Conversion and Management* **2009,** *50* (5), 1210-1217.https://doi.org/10.1016/j.enconman.2009.01.030.
[49] Fang, G.; Chen, Z.; Li, H., Synthesis and properties of microencapsulated paraffin composites with SiO_2 shell as thermal energy storage materials. *Chem Eng J* **2010,** *163* (1), 154-159.https://doi.org/10.1016/j.cej.2010.07.054.
[50] Lee, J.; Jo, B., Nanoencapsulation of binary nitrate molten salts for thermal energy storage: Synthesis, thermal performance, and thermal reliability. *Solar Energy Materials and Solar Cells* **2021,** *230*, 111284.https://doi.org/10.1016/j.solmat.2021.111284.
[51] Zhang, H.; Shin, D.; Santhanagopalan, S., Microencapsulated binary carbonate salt mixture in silica shell with enhanced effective heat capacity for high temperature latent heat storage. *Renew. Energy* **2019,** *134*, 1156-1162.https://doi.org/10.1016/j.renene.2018.09.011.
[52] Lee, J.; Jo, B., Surfactant-free microencapsulation of sodium nitrate for high temperature thermal energy storage. *Materials Letters* **2020,** *268*, 127576.https://doi.org/10.1016/j.matlet.2020.127576.
[53] Guo, P.; Qiu, Z.; Zhang, Y.; Zhong, H.; Zhao, X.; Zang, X.; Wang, D.; Shan, K., Preparation and characterization of phase change microcapsules for improving the applicable temperature and stability of high temperature resistant drilling fluids. *Chemical Engineering Research and Design* **2024,** *201*, 389-398.https://doi.org/10.1016/j.cherd.2023.11.054.
[54] Mo, S.; Mo, B.; Wu, F.; Jia, L.; Chen, Y., Preparation and thermal performance of ternary carbonates/silica microcomposites as phase change materials. *Journal of Sol-Gel Science and Technology* **2021,** *99* (1), 220-229.https://doi.org/10.1007/s10971-021-05563-5.
[55] Wu, W.; Zuo, H., Preparation and characterization of n-octadecane/poly(styrene–methyl methacrylate) phase-change microcapsule. *Journal of Thermal Analysis and Calorimetry* **2017,** *130* (2), 861-867.https://doi.org/10.1007/s10973-017-6470-6.
[56] Fatahi, H.; Claverie, J.; Poncet, S. Thermal Characterization of Phase Change Materials by Differential Scanning Calorimetry: A Review *Applied Sciences* [Online], 2022.
[57] Fu, K.; Mo, S.; Zhou, Z.; Li, Q.; Jia, L.; Du, Y.; Chen, Y., Enhancement of thermal characteristics of a novel stearic acid-adipic acid eutectic phase change material integrated with expanded graphite for thermal energy storage applications. *Journal of Energy Storage* **2025,** *121*, 116536.https://doi.org/10.1016/j.est.2025.116536.
[58] Cárdenas-Ramírez, C.; Gómez, M. A.; Jaramillo, F.; Fernández, A. G.; Cabeza, L. F., Thermal reliability of organic-organic phase change materials and their shape-stabilized composites. *Journal of Energy Storage* **2021,** *40*, 102661.https://doi.org/10.1016/j.est.2021.102661.
[59] Li, J.; Mo, S.; Xiao, B.; Li, Q.; Jia, L.; Chen, Y., A novel microencapsulated medium-temperature phase change material employing dicarboxylic acid for thermal energy storage. *Applied Thermal Engineering* **2024,** *255*, 123970.https://doi.org/10.1016/j.applthermaleng.2024.123970.
[60] Zhang, Z.; Jiang, Q.; Chen, M.; Diao, K.; Yang, M.; Zhu, Y., Experimental study of

erythritol – SiO_2 phase change nanocapsules for medium temperature thermal storage. *Applied Thermal Engineering* **2024,** *239*, 122167.https://doi.org/10.1016/j.applthermaleng.2023.122167.
[61] Zhang, Z.; Lian, Y.; Xu, X.; Xu, X.; Fang, G.; Gu, M., Synthesis and characterization of microencapsulated sodium sulfate decahydrate as phase change energy storage materials. *Applied Energy* **2019,** *255*, 113830.https://doi.org/10.1016/j.apenergy.2019.113830.
[62] Mo, S.; Xiao, B.; Mo, B.; Chen, J.; Jia, L.; Wang, Z.; Chen, Y., Improving the Thermal and Photothermal Performances of MXene-Doped Microencapsulated Molten Salts for Medium-Temperature Solar Thermal Energy Storage. *Energy & Fuels* **2023,** *37* (10), 7490-7500.https://doi.org/10.1021/acs.energyfuels.3c00508.
[63] Lu, J.; Deng, Y.; Luo, D.; Wu, F.; Dai, X., Preparation and performance enhancement of MXene/$Na_2HPO_4{\cdot}12H_2O$@SiO_2 phase change microcapsule. *Journal of Energy Storage* **2024,** *91*, 112079.https://doi.org/10.1016/j.est.2024.112079.
[64] Lee, J.; Jo, B., Synthesis and Thermal Performance of Microencapsulated Binary Carbonate Molten Salts for Solar Thermal Energy Storage. *Energy & Fuels* **2021,** *35* (17), 14130-14139.https://doi.org/10.1021/acs.energyfuels.1c01763.
[65] Ren, N.; Wu, Y.-t.; Ma, C.-f.; Sang, L.-x., Preparation and thermal properties of quaternary mixed nitrate with low melting point. *Solar Energy Materials and Solar Cells* **2014,** *127*, 6-13.https://doi.org/10.1016/j.solmat.2014.03.056.
[66] Geng, L.; Wang, S.; Wang, T.; Luo, R., Facile Synthesis and Thermal Properties of Nanoencapsulated n-Dodecanol with SiO_2 Shell as Shape-Formed Thermal Energy Storage Material. *Energy & Fuels* **2016,** *30* (7), 6153-6160.https://doi.org/10.1021/acs.energyfuels.6b00929.
[67] Ji, Y. H.; Jo, B., Detailed examination of the influence of surfactants on the thermal reliability of molten salt microcapsules for high-temperature latent heat storage. *Journal of Molecular Liquids* **2025,** *422*, 126950.https://doi.org/10.1016/j.molliq.2025.126950.
[68] Liu, S.; Sheng, W.; Zheng, H.; Pan, S.; Wang, Y.; Bayizi, M., Preparation and study of n-Tridecane@Silica low-temperature Nano-Encapsulated phase change microcapsules. *Energy and Buildings* **2025,** *334*, 115490.https://doi.org/10.1016/j.enbuild.2025.115490.
[69] Ghufran, M.; Huitink, D., Synthesis of silica-encapsulated myristic acid phase-change-assisted nanocapsules for thermal management applications. *Emergent Materials* **2024,** *7* (4), 1429-1443.https://doi.org/10.1007/s42247-024-00719-9.